Actin cytoskeletal and focal adhesion organisation in U2OS cells on polymer nanostructures

Jakob Vinje*[1], Noemi Antonella Guadagno[2], Cinzia Progida[2] and Pawel Sikorski[1]

[1]Department of Physics, Norwegian University of Science and Technology (NTNU)
[2]Department of Biosiences, University of Oslo (UiO)

Cells in their natural environment are embedded in a complex surrounding consisting of biochemical and biomechanical cues directing cell properties and cell behaviour. Nonetheless, *in vitro* cell studies are typically performed on flat surfaces, with clear differences from the more complex situation cells experience *in vivo*. To increase the physiological relevance of these studies, a number of advanced cellular substrates for *in vitro* studies have been applied. One of these approaches include flat surfaces decorated with vertically aligned nanostructures. In this work, we explore how U2OS cells are affected by arrays of polymer nanopillars fabricated on flat glass surfaces. We focus on describing changes to the organisation of the actin cytoskeleton and in the location, number and shape of focal adhesions. From our findings we identify that the cells can be categorised into different regimes based on their spreading and adhesion behaviour on nanopillars. A quantitative analysis suggests that cells seeded on dense nanopillar arrays are suspended on top of the pillars with focal adhesions forming closer to the cell periphery compared to flat surfaces or sparse pillar arrays.

1 Introduction

In vivo, cells typically reside in a a complex 3D environment called extracellular matrix (ECM). The ECM not only serves as a structural scaffold for the cells, it is also a conveyor of biomechanical and biochemical signals and thus regulates a range of processes such as tissue morphogenesis, homeostatis and differentiation. It is composed of water, polysaccharides and proteins[1, 2, 3, 4], and the composition varies between tissue types.

Motivated by the need of creating cell culturing models that better represent *in vivo* conditions, researchers have increasingly started to study cell behaviour also in 3D matrices and in "semi-3D" systems. A number of differences in cell phenotype between flat substrates and systems with higher dimensionallity have been identified [5, 6]. For example, characteristics such as viability, proliferation, differentiation and morphology are known to differ between cells on flat surfaces and cells embedded in 3D matricies[7, 3].

*jakob.vinje@ntnu.no

Despite this, planar culture plastic is most commonly used as an *in vitro* substrate for cellular studies. As cells on flat surfaces experience a remarkably different micro-environment than in living tissue, considerable effort has been put into development of advanced cell culturing platforms that better replicate *in vivo* conditions. *In vivo*-like substrates range from "semi-3D"/2.5D substrates, such as flat surfaces decorated with various nanostructures to "true-3D" systems such as collagen gels or matrigel matrices[8, 9, 10, 11]. In addition, controlled positioning of ligands on surfaces may give new insights into how cells interact with various chemical patterns[12, 13, 14].

Not only does the spatial properties of the surrounding structures differ, but also mechanical factors such as structure stiffness or even surface chemistry have been shown to influence cellular function[15, 16]. To this end, a large number of different substrates for cellular studies have been developed[3, 17]. Many systems with different physical structures and material compositions that mimic various aspects of the ECM have been realised[18, 19, 20, 21].

It has also been suggested that 3D culturing systems more precisely could predict the *in vivo* effect of a drug and thus these systems could find applications in drug discovery[16, 22, 23]. Precisely controlling nanoscale topographical patterns can also be used to regulate cell morphology. For example, wrinkles and grooves can be used to recreate the striated alignment of cardiomyocytes and thus better represent physiologically relevant conditions to model various diseases[24, 25].

The main adhesion used to connect the cytoskeleton of the cell to the ECM is facilitated by focal adhesions (FAs), a multiprotein complex including cell surface integrins and scaffold proteins. Through either inside out signalling or through environmental sensing, the transmembrane receptor integrin is recruited and form clusters in the cell membrane. Mechanical force is transmitted to the cell cytoskeleton from integrin adhesions through various adaptor proteins that bind to the actin cytoskeleton[26, 27, 28]. Depending on a complex set of regulatory mechanisms, the FAs form and disassemble at a turnover rate needed for forward movement, for example in cell migration. The FAs are known to exert mechanical force on the ECM, and conversely the ECM exerting force on the cells is known to influence integrin affinity and avidity in the membrane[29].

One of the proteins known to be an integral part of the FAs is vinculin. It is one of the linker proteins involved in anchoring F-Actin to the integrin-complex. Lack of vinculin alters cell morphology, adhesion and motility[30], and impairs the cells ability to transduce force to the substrate[31, 32, 33]. Vinculin is not only involved in the mechanical connection of the actin cytoskele to the integrin-complexes, it also has the ability to crosslink and bundle actin filaments[34, 35, 36], modify existing actin bundles[37], cap actin filaments, nucleate new actin polymerisation sites[38] and recruit actin modifiers[39].

Cells respond to the 3D matrices by changing the number and type of cell-substrate adhesion and induce changes in the spatial organisation of the cytoskeleton. These changes in turn influence distribution, size and dynamics of the formed adhesions[40, 4, 41, 42, 43]. This rearrangement may lead to changes in cell proliferation, morphology and motility[44].

In order to understand the influence of complex 3D environments on cells, there is a need to develop new model systems where cellular processes can be studied in 3D and compared to flat controls. As cellular response is known to depend on physical, mechanical and chemical characteristics of the culturing substrate, it is desirable to fabricate cellular substrates with precisely controlled properties[45, 46, 47]. Additionally, it is highly advantageous if the cells and the substrate easily can be studied using already established analysis techniques such as optical microscopy.

One type of substrate that has recently gained attention are flat surfaces decorated with nanopillars or nano-wires[48, 49, 50, 51, 17, 52, 53, 54, 20, 55]. Compared to for example hydrogels, these structured surfaces do not mimic the true 3D environment, but have well defined surface topography. These substrates are typically referred to as being 2.5D. Such systems have already been applied to facilitate delivery of biologically relevant molecules into cells[56, 57], to monitor enzymatic activity[58], to test nuclear mechanics[59] and to study how tuning the membrane curvature influence various cell-membrane related processes[60, 61, 62]. By fabricating nanostructures

on transparent substrates, it is possible to integrate this approach with optical microscopy.

In previous work we have described detailed protocols for fabrication of SU-8 polymer nanostructures on flat glass surfaces[63], and explored cell behaviour for two different cell lines on these surfaces[50, 47]. In this work, we use electron beam lithography (EBL) to fabricate surfaces decorated with vertically aligned SU-8 polymer structures to study changes in actin cytoskeletal and FA organisation in the osteosarcoma epithelial cell line U2OS. We perform both qualitative and quantitative analysis of the changes induced by the surface with different topological cues

2 Materials and Methods

2.1 Fabrication of nanostructures and sample mounting

SU-8 nanostructures were fabricated as previously explained[63]. Briefly, 24 mm by 24 mm glass cover slips (#1.5, Menzel-Gläser, thickness 170 µm) were cleaned by immersion in acetone, isopropyl alcohol, rinsed in de-ionised water and dried. The cover slips were then oxygen plasma treated for 2 min (Diener Femto plasma cleaner, power 100 W, base pressure 0.3 torr), followed by dehydration for 10 min on a 150 °C hot plate. Samples were then placed in a desiccator containing an open vial of Hexamethyldisilazane (HMDS, Sigma Aldrich product no: 440191). HMDS was applied by vapour deposition, the desiccator was pumped to low vacuum using a diaphragm pump for 5 min and the samples were kept in HMDS atmosphere for 60 min.

Substrates for EBL were prepared directly after HMDS treatment by spin coating SU-8 2001 (Microchem Corp.) to a desired thickness of 500 nm and 1000 nm. SU-8 was made fluorescent by adding either Oxazine 170 perchlorate, Rhodamine 800 or Coumarin 102 (all Sigma Aldrich) to a final concentration of 100 µg mL^{-1} resist. After spin coating samples were dehydrated on a hot plate at 95 °C. To mitigate charging during EBL exposure samples were then covered by a layer of conductive polymer AR-PC 5091 Electra 92 (AllResist GmbH) by spin coating at 2000 rpm for 60 s to thickness of 50 nm.

Table 1: Summary of fabricated surfaces studied in this work. Structure height is corresponding to the thickness of the spin coated SU-8 film, whereas array pitch is the separation between the exposure position for each of the pillars in the array. The exposure time given is the rate at which an array could be exposed and does not take any other processing steps into account.

Structure height	Array pitch	Exposure time
500 nm	500 nm	0.7 mm^2 / min
	1000 nm	1.5 mm^2 / min
1000 nm	750 nm	0.9 mm^2 / min
	1000 nm	1.5 mm^2 / min
	2000 nm	4.0 mm^2 / min

An Elionix ELS-G100 100 kV EBL-system was used to fabricate SU-8 nanopillars (NPs) with processing parameters as described in our previous work[63]. Table 1 summarise the arrays fabricated for this work. Pillar arrays were exposed using the Elionix dot-pattern generator where each pillar is exposed in a single exposure. Arrays were exposed over an area of 2000 µm by 4000 µm, with a current of 500 pA in write fields of 500 µm by 500 µm. NPs had a tip diameter of about 100 nm as a base diameter of 150 nm and 200 nm for structures of length 500 nm and 1000 nm respectively.

After EBL exposure, the samples were rinsed in DI-water to remove the conductive polymer, then post exposure baked for 2.3 min at 95 °C and developed twice in mr-Dev 600 (Micro Resist

Technology GmbH) developer for 20 s, rinsed in isopropyl alcohol and dried. Samples were then treated with oxygen plasma (Diener Femto plasma cleaner, power 50 W, base pressure 0.3 torr) for 30 s to render SU-8 hydrophilic.

Fabricated structures were imaged using Scanning electron microscopy (SEM) and samples sputter coated with 5 nm Platinum/Palladium alloy deposited with a 208 HR B sputter coater (Cressington Scientific Instruments UK). SEM was performed with a FEI Apreo SEM, at 5 kV and 0.2 nA with sample 45° pre-titled stage and with additional tilting of 30°.

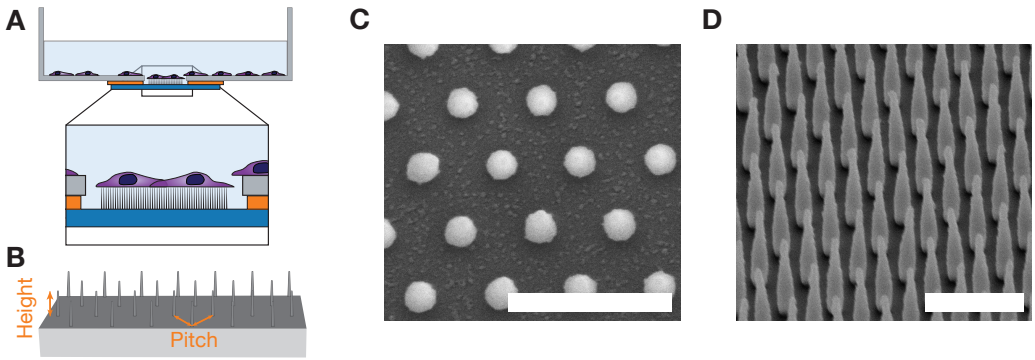

Figure 1: A) Side view schematic representation of nano-structured surface mounted in petri dish. Glass slides are mounted using paraffin such that structures are pointing upwards. B) Tilted schematic representation of nano-pillar array on flat surface, and two important parameters for the nano-pillar arrays (height and pitch). These figures are not drawn to scale. C-D) Overview of the nanopillar arrays employed in this work. Top-down and tilted side-view scanning electron micrographs of fabricated nano-pillar array with pillars of height 1000 nm and pitch 1000 nm. Scalebars 2000 nm.

When exposing the pillars, an indexing system was also exposed to make navigation during live-cell imaging more reliable. Arrays were optically inspected after fabrication to ensure free and standing pillars. The short Oxygen plasma treatment to render the SU-8 structures did not lead to any optically visible change to the structures. Lastly, the samples were mounted underneath 35 mm diameter dishes (Cellvis, Mountain View, CA, USA) with 14 mm holes and nano-structures pointing upwards, as indicated schematically in Figure 1. For flat glass surfaces, 35 mm imaging dishes with a 14 mm glass well was used directly. Before usage, all dishes with mounted samples were disinfected with 70% ethanol twice and dried.

2.2 Cell culture and transfection

U2OS-cells (ATCC) were cultivated in Dulbecco's modified Eagle's Medium (DMEM Prod. 41965039, Fischer Scientific) with 10% fetal bovine serum (FBS) and kept at 5% CO_2 and 37 °C. Before detachment, cells were washed with PBS and detached with Trypsin-ethylenediaminetetraacetic acid (trypsin-EDTA) and seeded on nanostrucutred or flat surfaces. For the diameter 14 mm glass wells 15 000 cells were seeded.

For the standard transfection experiments, cells were allowed 6 h for adhering to surfaces before transfection. U2OS cells were transiently transfected using Lipofectamine 2000 (Invitrogen, Fischer Scientific) by adapting the manufacturer protocol to our system. Briefly, 2 µL Lipofectamine 2000 was added to 50 µL Opti-MEM I Reduced Serum Media (Prod. 11058021, Gibco , Fischer Scientific) and incubated for 5 min at room temperature. Plasmid DNA coding for fluorescent actin-GFP and TagRFP-vinculin fusion proteins were co-transfected by using 0.5 µg plasmid DNA (pTagRFP-vinculin and pCMVLifeAct plasmids) was diluted in 50 µL Opti-MEM I and incubated at room

temperature for 5 min. For co-transfection of TagRFP-vinculin and pCMVLifeAct 0.5 µg of each plasmid was used.

The diluted DNA was added to the diluted Lipofectamine 2000 in a 1 : 1 ratio, and left to incubate for 20 min at room temperature. 40 µL of the combined transfection complex was then added to each well. After 18 h, 1.5 mL DMEM (Prod. 41965039) supplemented with 10% FBS and 1% 10 000 U/mL Penicillin-Streptomycin was added to each dish.

For reverse transfection experiments, the same amounts of reactants were used, but the transfection complex was added to a suspension of U2OS cells, and the suspension was then added to the wells.

2.3 Microscopy

Live cell imaging was performed using a Zeiss LSM 800 Airyscan with an inverted Axio Observer Z1 stand connect to a PeCon compact incubator. Imaging was performed in an humidified environment at 37 °C, with 5% CO_2 flow. High resolution imaging was performed using a Zeiss Plan-Apochromat 63x/1.4NA DIC M27 oil objective with Cargille Immersion Oil Type 37 (n = 1.51) suited for use at 37 °C. All images were taken using the system optimised pixel size both in-plane (typically 34 nm) and for stacks in the vertical axis (typically 180 nm).

To minimise imaging bias, imaging was performed in a standardised manner where each pillar array was raster scanned and cells expressing both F-Actin GFP and Vinculin RFP were imaged. The high resolution images were then processed using a Zeiss algorithm for reconstruction of AiryScan images and exported as CZI-files for further manual and automatised image processing.

2.4 Image analysis

For all cells, cell shape was based on the expression GPF-actin fusion protein and expression of TagRFP-vinculin was used to identify FAs. Segmentation of images was performed using a script written in Python 3[64] using CZIfile[65] (version 2017.09.12) for reading the microscopy images in Zeiss-format. The python packages Scipy[66] and Scikit-image [67] were used for multi-dimensional image processing and image segmentation respectively.

To reduce the influence from fluorescence cross-talk from pillars (due to Oxazine 170 perchlorate, Rhodamine 800 or Coumarin 102), the pillar/surface channel was used as a background and subtracted from the TagRFP-vinculin imaging channel. A median filter (size: 10 pixels) was applied to remove noise from the TagRFP-vinculin channel, followed by classification of the image into regions based on their intensity value using a Multi-Otsu approach. Multi-Otsu thresholding with three classes was applied. The first class was typically the background, the second class constituted the cytosolic vinculin, whereas vinculin rich areas in FAs appeared brighter and could be classified into a third class.

Area of cells and vinculin rich regions were described by counting pixel numbers and from this the actual area was found by correcting for the pixel size. Shape geometries were described by fitting each region with an ellipse with the same second-moment as the segmented region. In order to describe the cell area geometry, three measures were used: 1) Aspect ratio defined as the ratio of the ellipse major axis to the minor axis. 2) Circularity given as,

$$C = \frac{4\pi * \text{Area}}{\text{Perimeter}^2}, \tag{1}$$

and Roundness given as,

$$R = \frac{4 * \text{Area}}{\pi * \text{MajorAxis}^2}. \tag{2}$$

Segmented vinculin areas with a fitted ellipse that were too round (aspect ratio ≤ 1.5) or too elongated (aspect ratio ≥ 8.5) were rejected. In order to find the distance between each vinculin area and the cell edge, the shortest euclidean distance between each centroid (the centre of the fitted ellipse for each vinculin area) and the cell edge was calculated.

2.4.1 Statistical analysis

Statistical comparisons of distributions were performed by using the non-parametric two-tailed Mann-Whitney test neither assuming normal distribution nor equal standard deviation. P-values ≥ 0.05 were considered to represent a non-significant (ns) difference between the two populations. Significant values were denoted with * for p in 0.01 to 0.05, ** for p in 0.001 to 0.01, *** for p in 0.0001 to 0.001 and lastly **** for $p \leq 0.0001$.

3 Results

Using previously established protocols, we have fabricated glass cover-slips decorated with precisely defined arrays of vertically oriented SU-8 nanopillars (NP) with variable separation and defined geometry[63]. These surfaces with NP densities of 456, 205, 115 and 29 NPs/100 µm^2 (corresponding to pitches of 500 nm, 750 nm, 1000 nm and 2000 nm) were used to investigate the nanostructure induced changes to morphology, distribution of focal adhesions (FAs) and actin cytoskeleton structure of U2OS cells. Figure 1 shows a schematic representation of the NP arrays and electron microscopy images of fabricated substrates. To be able to detect NPs in confocal microscopy, SU-8 was doped with either Rhodamine 800 or Coumarin 102.

Table 2 shows geometric parameters of arrays used in this work, their classification, as well as the corresponding NP area number density. We classify NP arrays into dense and sparse depending on observed cell adhesion behaviour (see below).

Table 2: Overview over pillar arrays used for the study of actin organisation and FA localisation in this work. Arrays with a given structure height and array pitch are categorised into being either Dense or Sparse and the corresponding density of NPs is reported.

Height	Array pitch	Category	Density
500 nm	500 nm	Dense	456 NPs/100 µm^2
	1000 nm	Sparse	115 NPs/100 µm^2
1000 nm	750 nm	Dense	205 NPs/100 µm^2
	1000 nm	Dense	115 NPs/100 µm^2
	2000 nm	Sparse	29 NPs/100 µm^2

Figure 2 shows representative U2OS cells cultured on glass (A) and nanostructured surface (B-F) for 24 h. The cells have been co-transfected with pCMV-LifeAct-GFP and pTAG-RFP-Vinculin, that results in production of flourescent actin-GFP and TagRFP-vinculin fusion proteins. F-actin network and vinculin rich areas in FAs are clearly detected. At the cell periphery, the actin signal is in close proximity to the membrane and therefore we use the this signal to visualise cell morphology. Signal from SU-8 NPs that contain a fluorescent dye is shown in blue (see Experimental section).

Preliminary tests where transfection complex was added to cells prior to seeding, showed that cells seeded on both glass and structured surfaces appeared to be fully spread after approximately 6 h with FAs initially forming on, around and in between pillars (see Supplementary Information for cells on some example surfaces). Therefore, in the following experiments cells were transfected 6 h after seeding and imaged 24 h and 48 h after transfection, as the preliminary tests also showed that

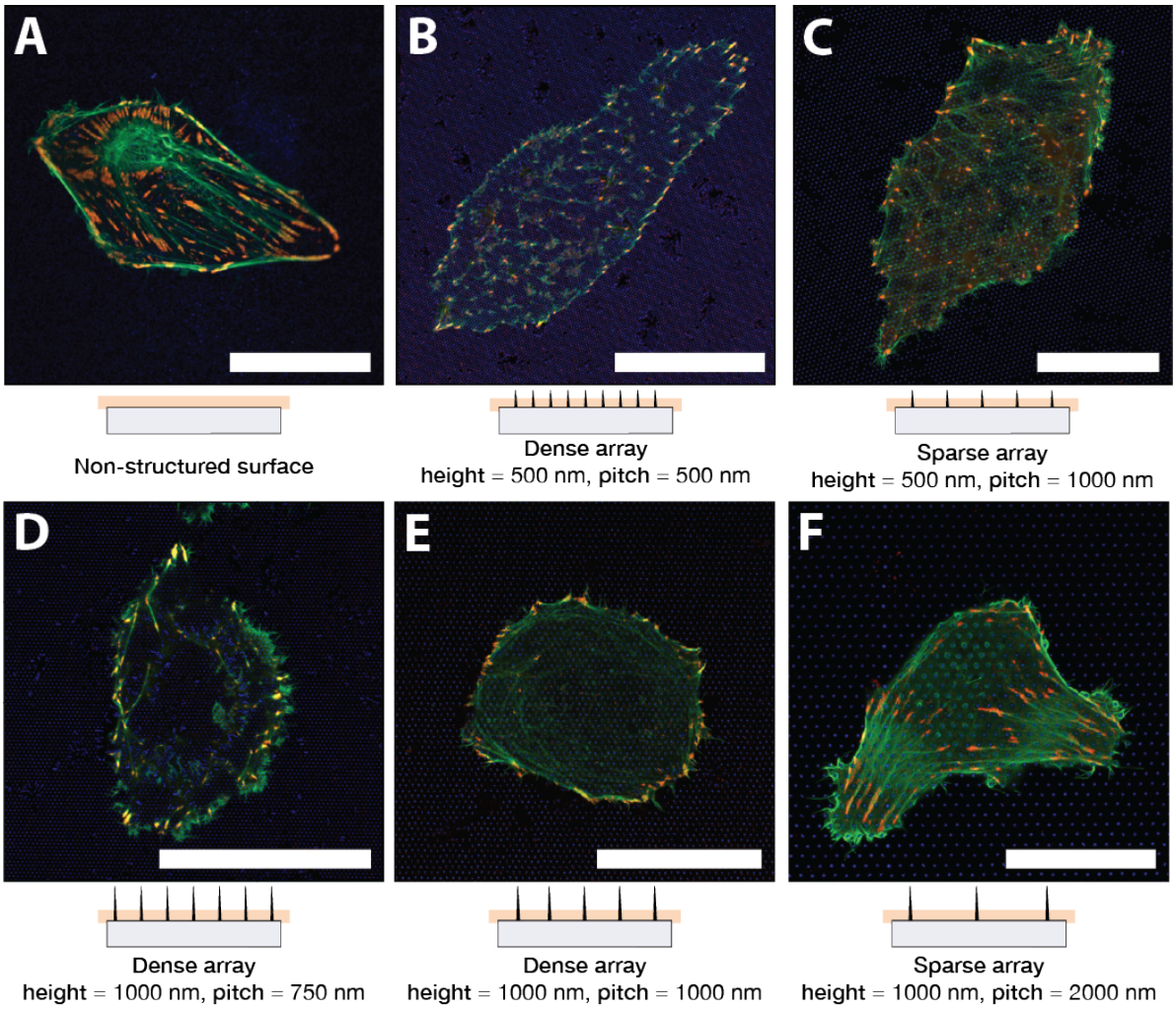

Figure 2: U2OS expressing fluorescent actin-GFP (green) and TagRFP-vinculin (red) spreading on different surface types. Yellow colouring indicates overlapping signals from actin-GFP and TagRFP-vinculin channels. Below each micrograph a schematic side-view of the corresponding NP array is shown, as well as the appriximate height the image was acquired at. Cells imaged on A) non-structured flat glass surface and on pillar arrays with different densities and structure heights: B) 500 nm pitch and 500 nm height, C) 1000 nm pitch and 500 nm height, D) 750 nm pitch and 1000 nm height, E) 1000 nm pitch and 1000 nm height, and F) 2000 nm pitch and 1000 nm height. All images presented are of representative cells. Scalebar 25 µm.

sufficient and consistent expression of fluorescent actin-GFP and TagRFP-vinculin was observed after approximately 24 h.

No evident differences in the initial cell spreading for cells seeded on NP arrays with height 500 nm and 1000 nm and pitch 750 nm, 1000 nm and 2000 nm were observed. After the initial spreading, cells were observed to be either round or more elongated, similar to the situation on flat surfaces. This general morphology of the cells were also found to be consistent over multiple experiments.

Cells seeded on sparse NP arrays generally have a shape similar to the cells on glass surface, see Figure 2F depicting a representative cell on a 2000 nm pitched array. For cells on sparse arrays, F-actin was present also at the base of the NPs and in proximity of the glass surface in-between pillars, indicating that the cell membrane is able to fully wrap around the NPs and the cell is able contact the glass surface in-between NP. As observed previously[68, 69, 47], cells on dense arrays, typically appear to be suspended on top of the NP arrays (Figure 2B,Figure 2D and Figure 2E), whereas on sparse arrays, the cells are able to contact the surface in-between NPs (Figure 2C and Figure 2F). The relation between NP height and separation appears to be determining for which state is observed. This is shown in Figure 2B where shorter NPs lead to the cell being able to contact the substrate, whereas longer NPs hindered contact, Figure 2E. The ability of the cell to contact the surface can be explained by the limited ability to deform the cell membrane and underlying proteins leading to a limited ability for the cell membrane to conform to the relatively deep gaps between NPs.

To get a more detailed understanding on how cells adhere to the structured and non-structured surface, we evaluated distribution of vinculin-rich FAs as visualised by the presence of TagRFP-vinculin fusion protein. Cells on flat surfaces typically formed elongated FA distributed underneath the whole cell body, as shown in Figure 2A.

On sparse arrays, U2OS were able to contact the glass surface in-between NP and adhered similarly to cells on glass. Figure 2F shows a representative cell 24 h after seeded on the surface. For this NP array, FAs formed in-between NPs, and the F-actin signal was also detected in the image acquired close to the base of the NPs, hereby indicating that the cells were able to bend the membrane around the nanostructures and contact the surface. Cells on denser arrays however, such as 750 nm and 1000 nm separation and 1000 nm height, are clearly hindered from adhering to the substrate between the nanostructrues, as shown in images Figure 2D and Figure 2E acquired close to the base of the NPs. However, around the periphery, the cells are typically able to attach to the substrate between the nanostructures forming FAs, often directed by the symmetry of the underlying pillar array.

Cells spreading on NP arrays with shorter length, and with an inter-pillar spacing of 1000 nm formed adhesions both towards the periphery and more centrally in the cell. Also for this surface type, the F-actin fibre orientation was directed by the symmetry of the underlying array, as shown in Figure 2C. However, the location and orientation of vinculin containing FAs did not exhibit any clear pattern, with FA forming in-between NPs.

U2OS cells on 500 nm pillars with inter-pillar distance of 500 nm generally formed fewer and smaller adhesions compared to the planar surface as shown in Figure 2B. For cells seeded on this array, actin fibers were only able get in proximity with the glass surface at positions where they terminated in FAs. Again, this is a sign that the cell is mostly hindered from contacting the surface and is mostly suspended on top of the dense array. However, cells appeared to have more continuous F-actin forming in areas of the cells not confined by NPs. Cells imaged on this dense array also appeared to be align with structures in the underlying array. This is seen by F-actin fibres and FAs predominantly forming parallel to one of the lattice directions given by the hexagonally ordered pillars, in other words in between the pillars.

On both dense and sparse arrays, we observe "ring-like" F-actin structures forming around NP that protrudes upwards into the cell body. The formation of F-actin rings around NP has previously

been described for fibroblasts on similar surfaces[47] and for U2OS cells on nanostructures with a range of structure sizes[60].

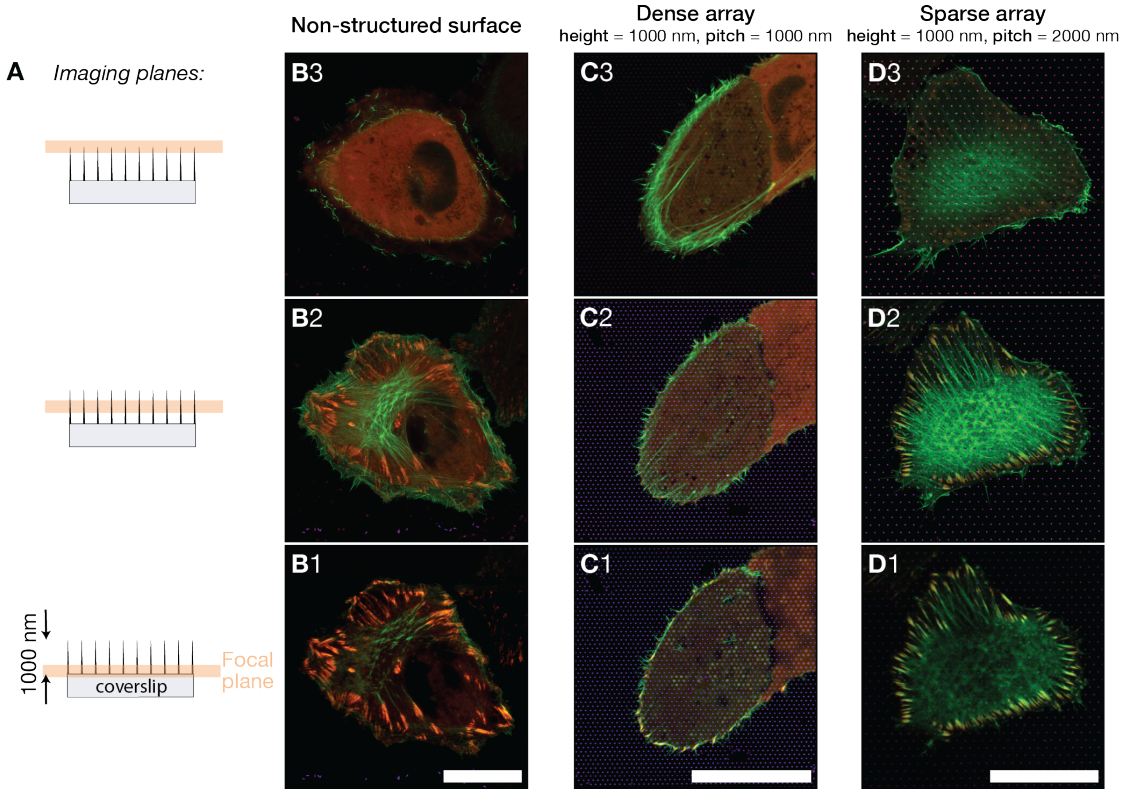

Figure 3: A) Imaging of U2OS cells spreading on different surfaces were acquired at three focal heights, with the approximate focal plane position shown.The location of the plane relative to the NP are indicated. Images were obtained close to the pillar base, approximately at half-pillar height, and close to the pillar apex. For flat non-structured surfaces (glass) there were no pillars, but imaging was performed at the same relative height. B,C,D) Merged fluorescence images showing U2OS expressing fluorescent actin-GFP (green) and TagRFP-vinculin (red) spreading on different surface types, yellow colour is indicative of overlapping actin-GFP and TagRFP-vinculin. Imaging was performed at the z-positions indicated by the illustrations in A). Imaged surfaces were B) non-structured glass surface, C) 1000 nm pitched pillar array, D) 2000 nm pitched pillar array. Presented images are representative for cells on the surfaces. The vertical distance between each image shown is approximately 400 nm. Scalebars 25 µm for all images.

Based on the outcome of the microscopy we selected three surfaces for a more detailed and quantitative description of cell morphology and location and shape of FAs. We chose the following three surfaces to analyse further: 1) a dense pillar array (array pitch 1000 nm), 2) a sparse array (pitch 2000 nm) both arrays with NP length 1000 nm, 3) a flat glass control surface.

By employing the Airyscan detector together with the dedicated image post-processing, we were able to perform imaging with an xy-resolution of about 140 nm and z-resolution of about 400 nm[70]. Figure 3 shows images of cells on the three surfaces, with imaging planes separated by approximately 400 nm. These detailed stacks support the initial observation that cells on sparse arrays attach the surface between the structures, whereas cells on dense arrays are primarily able to attach around the cell periphery.

To analyse and quantify the differences in FAs and cell morphology for the three selected surfaces

a Python based image analysis script was written. For the quantitative analysis, more than 300 high-resolution images were analysed. In these images, > 400 cells and > 7700 FAs were identified, Table 3 lists the number of detected cells and FAs for the three surface types included in the analysis. For all surfaces, cells were imaged both 24 h and 48 h after transfection. Calculated geometrical parameters from detected cells such as surface area, circularity and aspect ratio did however not differ significantly and in the following analysis data from the two populations are combined into one. Surface area, circularity and aspect ratio for cells and FAs are shown in Figure 4, and values are listed in Supplementary Information. The parameters were defined as described in the Experimental section.

Table 3: Number of observations for cells (n_{cell}) and for FAs (n_{FA}) used in the quantitative analysis. Reported values correspond to the total number of cells identified by the image analysis script for each combination of time (24 h and 48 h) and surface type (flat surface, 1000 nm pillar array and 2000 nm pillar array).

Surface	Time [h]	Observations	
		n_{cell}	n_{FA}
Flat	24	29	1379
	48	69	1280
Pillars 2000 nm	24	121	2513
	48	94	1307
Pillars 1000 nm	24	80	814
	48	30	451

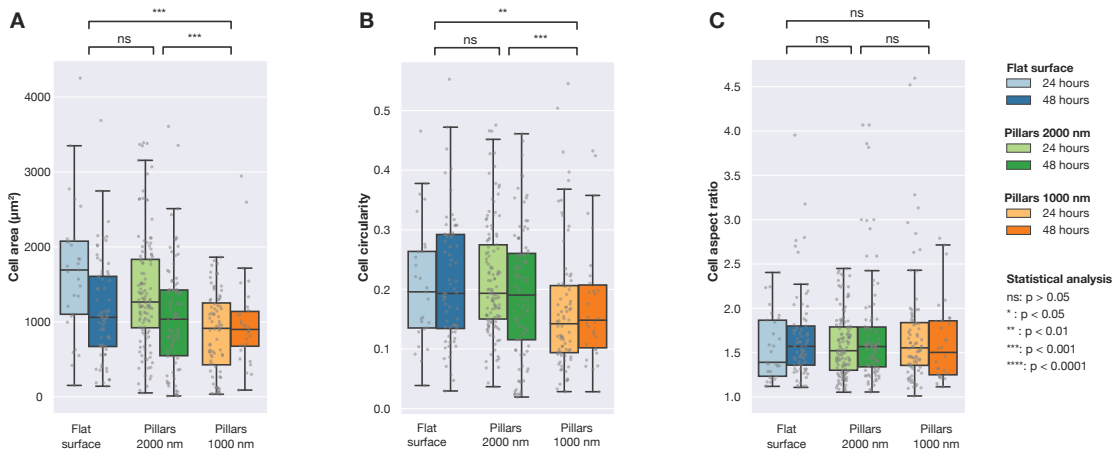

Figure 4: Calculated cell area, cell circularity and cell aspect ratio for U2OS cells expressing floures-cent actin-GFP and TagRFP-vinculin fusion proteins on different surfaces imaged 24 h and 48 h post-transfection. The image detection was performed based on the intensity of the expressed actin-GFP signal. Each grey point correspond to an observed cells and the box plots shown median values ($Q2$) as well as the first ($Q1$) and third quartile ($Q3$). Statistical differences between the distributions were assessed using the Mann-Whitney non-parametric test.

Figure 4 summarises data collected for both flat and structured surfaces. As shown in Figure 4A there were no differences in average surface area of cells seeded on flat surfaces compared to sparse arrays. Cells on dense arrays however, had significantly reduced area. The trend is similar when the average cell circularity is considered (Figure 4B): cells on flat surfaces and sparse arrays showed

similar circularity, whereas cells on dense surfaces had significantly lower average cell circularity compared to cells on flat surface or sparse arrays. Cells on all three surfaces had the same aspect ratios, as presented in Figure 4C. Cells were imaged both 24 h and 48 h after transfection, and the statistical analysis presented in the figure considers the two populations for each surface as one.

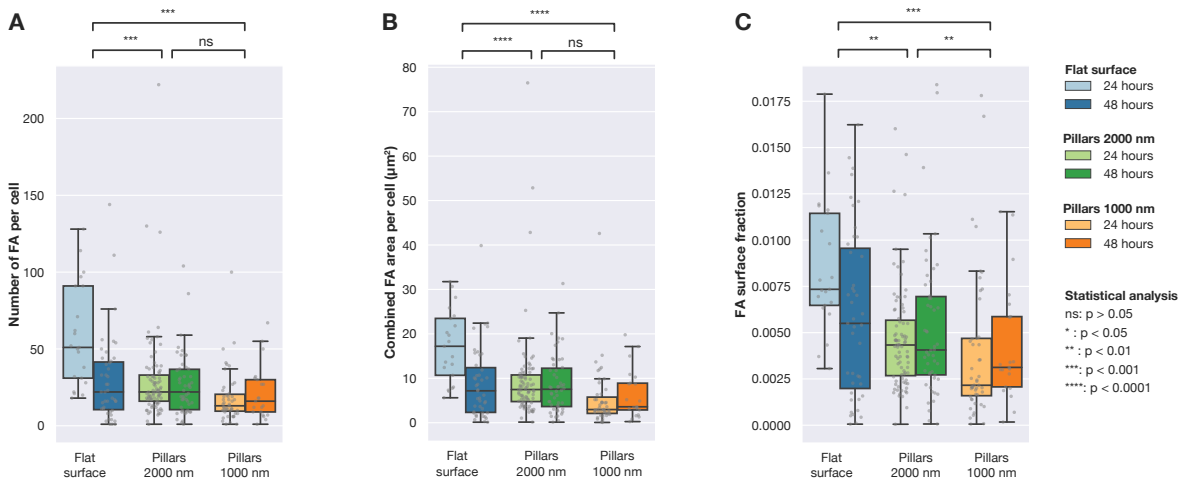

Figure 5: Number of FAs, combined FA area per cell and fraction of FA area to cell area shown for cells imaged on the different surface types (flat and pillar arrays with pitches of 1000 nm and 2000 nm). Each grey point corresponds to either A) the number of FAs in each cell, B) the summed detected area of all adhesions in each cell or C) the summed FA area for each cell relative to the detected area of that cell. Statistical significance between the distributions was determined using Mann-Whitneys non-parametric test.

Figure 5 shows the distribution of the number of detected FAs per cell, total surface area of FAs in each cell and the ratio of FA area to cell area. The total number of FAs formed by cells on sparse and dense arrays were significantly lower than the number formed on flat control surfaces. As shown in Figure 5B, the total FA surface area per cell also differs for cells seeded on flat and structured surfaces, but without any significant difference between cells seeded on dense and sparse arrays. However, as shown in Figure 4 cells on dense arrays spread significantly less than on sparse arrays. Due to the lower cell area, the relative amount of FAs (the total area of detected FAs divided by the total cell area) show significant differences between the cells on different surfaces. This is shown in Figure 5C. We observe that there are clear changes in the cell adhesions when the cells interfaced with nanostructured surfaces. However, the distribution of size and shape of single FAs are not different across surface types, as shown in Supplementary Information. The differences between cells on different surfaces lies mainly in the number of FAs being different.

Analysis on a per-cell basis show that cells on pillar arrays have a significantly lower number of detected FAs per cell as shown in Figure 5A. The decrease in FA area for cells on pillars is also evident when looking at the total FA area per cell (see Figure 5B) or on the surface fraction that the FAs corresponded to for each cell (see Figure 5C). We observe that there are significant changed in FAs when the cells were seeded on dense arrays of nano-pillars.

To understand how the whether the presence of NPs influence the localisation of FAs in the cell, we performed further analysis using the location of the FAs. Microscopy data indicated that FAs in cells on dense NP arrays were located closer to the cell periphery, as indicated by Figure 2 and Figure 3. To quantify this trend, we calculated the shortest distance from each FA to the cell edge. This was performed as illustrated in Figure 6. F-actin was used to determine location of the periphery and by constructing distance maps, the distance between each centre of a detected FA to the cell periphery was calculated. Data is presented in Figure 7 and Table 4. For cells on flat

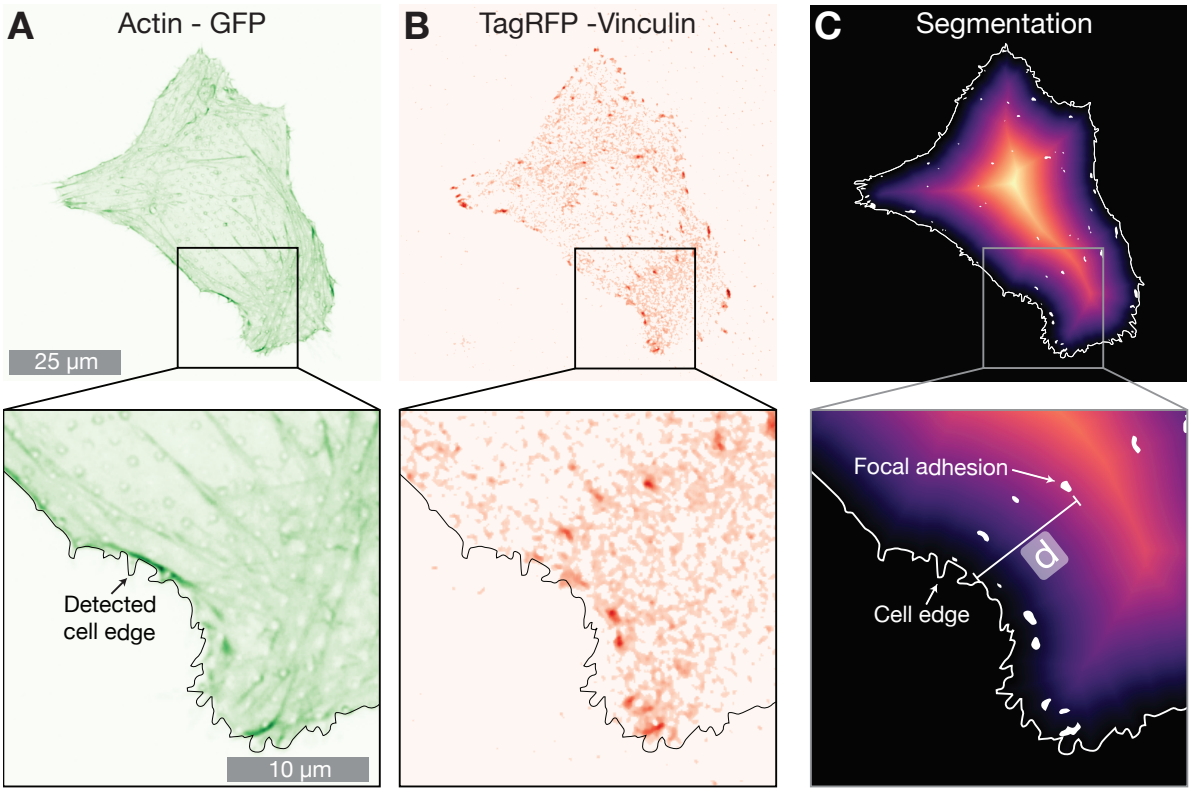

Figure 6: Example cell on 2000 nm pillar array expressing A) actin-GFP (green) and B) TagRFP-vinculin (red). Superimposed on both figures is the detected cell edge determined by using the signal from expression of actin-GFP (as shown in A). C) Shows a distance map from the detected cell edge as well as detected FAs. The shortest distance (denoted with d in figure) from each segmented vinculin spot (white areas) to the cell periphery (indicated with a solid white line) was calculated for all FAs in the images.

surfaces, the FAs are distributed more towards the centre of the cell, whereas on both on sparse 2000 nm arrays and dense 1000 nm arrays, the FAs are located closer to the cell periphery. This effect is most notable for dense arrays with 1000 nm pitch.

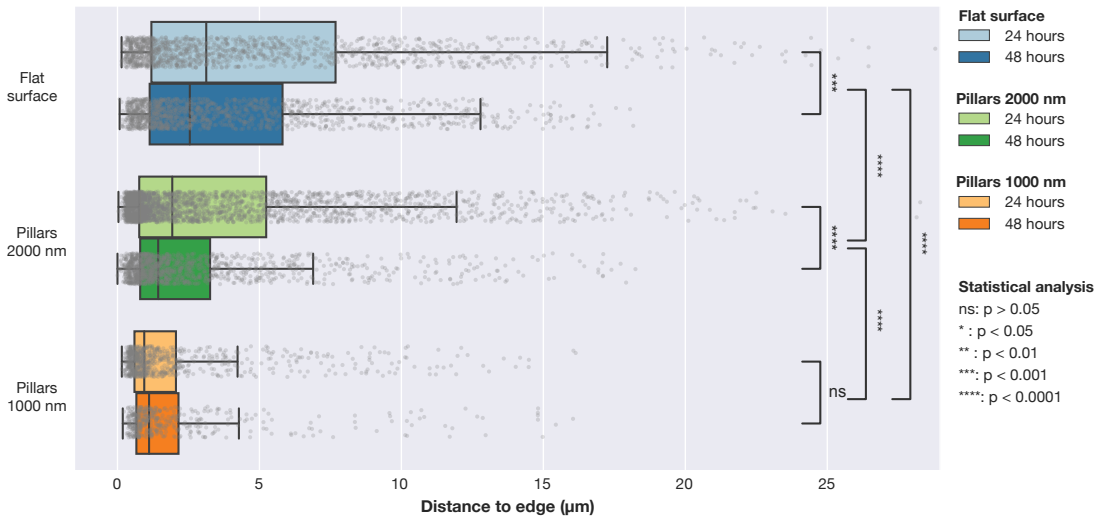

Figure 7: Distribution of FAs positions in relation to the closest cell edge. Distances was measured by calculating the distance from each observed FA to the cell edge defined by the actin GFP signal and plotted for the three surface types at 24 h and 48 h. Grey points represent individual observations of FAs and their distributions are summarised in the box plots. To test the likelihood that the FAs from the different surfaces and time points were from the same distribution, Mann-Whitney tests were perforbmed on all distributions with significance levels denoted in the figure.

Table 4: Distance from the centre of a detected FA to the closest edge of cell defined by the F-actin-GFP signal. Number of observations used in analysis is given as n_{FA}. Values reported for the distance are median values ($Q2$) as well as the first ($Q1$) and third quartile ($Q3$).

Surface	Time [h]	n_{FA}	Distance [µm^2]
			$Q2\,[Q1, Q3]$
Flat	24	1379	3.127 [1.194, 7.681]
	48	1280	2.548 [1.133, 5.814]
2000 nm	24	2513	1.930 [0.766, 5.238]
	48	1307	1.434 [0.799, 3.262]
1000 nm	24	814	0.943 [0.598, 2.059]
	48	451	1.113 [0.666, 2.149]

4 Discussion

Organisation of actin cytoskeleton and formation of adhesions are processes studied extensively on flat surfaces. The present study was designed to investigate the changes in organisation of the actin cytoskeleton and focal adhesions (FAs) when the geometry of nanopillars (NPs) was introduced as a factor. From our results using transiently transfected U2OS on polymer nanostructures, we have identified that there are characteristic changes in both actin and FA organisation comparing NP arrays to flat surfaces.

Allowing the cells spread and adhere on the surfaces for an extended period of time (1 or 2 days) before imaging makes it possible to view the actin cytoskeleton organisation and the presence of fully matured FAs. Imaging cells after an extended period of time corresponds to imaging the "steady state" of the cell on the surfaces, potentially overlooking processes occurring before the cells have fully spread and the FAs have matured. For example we speculate that cells initially form FAs closer to or on the pillars, in particular for dense arrays. Yet this is not seen in our analysis, and we hypothesise that over time the cells no longer has a preference of forming FAs on the pillars.

Changes actin cytoskeleton organisation are also connected to changes in how a cell interacts with the surroundings. For example, integrin based FAs are predominantly promoted by stress fibres[71]. Others have reported rounder cells/lower aspect ratio and FA localisation around edges for cells seeded on soft/compliant surfaces. [72]. In our results we see similar trends, most likely since the NP array could be regarded as somewhat compliant as the cells are able to detach the NPs around the cell edges. This is mainly observed for cells suspended on top of the NPs on dense arrays. For sparse arrays, the distribution of FAs throughout the cells appear to interfere in the formation of edge fibres and FAs around the cell periphery, leading to a smaller number of detached pillars. Despite this, the same effect could be achieved by only increase in higher torque from the cells to the NPs when they are suspended on top of the NP array.

The interaction between FAs and actin cytoskeleton is complex and still not fully characterised. FAs linking the actin cytoskeleton to the ECM is known to act as traction points and to promote stress fibre formation in the cells. Conversely, actin fibres are again influencing the organisation and maturation of FAs.

Numerous studies describe how cells tend to be suspended on top of dense NP arrays[69, 73] and how cell membranes interact with single NPs[74, 75, 76]. These observations are corroborated by theoretical studies[68] and the cellular behaviour on pillars is fairly well understood.

The mechanism behind the cellular attachment around the edge on dense arrays, however, remains unclear. One possibility is that this effect is caused by an increased cell pliability around the periphery of the cell due to a lower presence of membrane stiffening proteins. This could make it easier for the cells to form FAs closer to the cell edge, as seen in our results. Another possibility is is that the lower cytoskeletal rigidity around the cell periphery allows for a more readily available plasma membrane reservoir access[77].

There are also studies describing the effect FA placement has on cells[43]. By modelling cells on planar substrates Stolarska et al. suggest that the cells can control intra-cellular stresses by three mechanisms: FA position, FA size and attachment strength. Proposed is that FA localisation around the periphery allows the cells to be more sensitive to changes in the micro-environment. This could also be an underlying mechanisms for cells on NPs. Yet, it is not obvious that the results for the planar substrate are directly transferable to NP decorated surfaces.

It is clear for our results that NP arrays influence the organisation of the actin cytoskeleton and the localisation of FAs compared to flat surfaces. Changes in the actin network are also linked to alterations in the cell interaction with surrounding, for example through an increased formation of stress fibres known for promote the formation of FAs[71]. Cell-interactions with the surroundings, if flat substrate, NPs or *in-vivo* ECM, are regulated by a complex set of relations between actin organisation, membrane mechanics, cell dynamics and contact with FAs. To further explore these relations, applying flat surfaces structured with NPs could be one promising approach.

5 Conclusion

In order to create more physiologically relevant systems for cellular studies, a plethora of 3D and 2.5D approaches have been proposed. One approach is to use flat-surfaces decorated with vertically aligned nanostructures as a simple model system. High resolution live cell imaging of

co-transfected U2OS cells expressing pCMV-LifeAct-GFP and pTAGRFP-Vinculin have been used to study the influence of nanopillar arrays on actin cytoskeleton focal adhesion organisation. Our present results indicate that the U2OS cells spreading on surfaces decorated with nanopillars can be categorised into three different regimes by how they respond to the nano-structures. These observed changes are quantified by analysing more than 400 high-resolution images, and indicate that tuning geometrical properties of the nanostructured surface can be used to direct cell behaviour.

Increased understanding of how cells behave on nano-structured surfaces, such as pillar arrays, could help us discover more details about complex cellular processes. For example, it is still poorly understood how changes in the actin cytoskeleton and its architecture influence cell signalling. By studying the cell response on nanostructured surfaces in a systematic way, the potential connection between actin cytoskeleton, cell adhesions and a plethora of biochemical signalling pathways could be further explored. We therefore envision that further development of the presented platform and analysis could have implications for advanced *in vitro* applications or for development of smarter *in vivo* biointerfaces.

Acknowledgements

Irene Persiconi (Department of Biosciences, UiO) is acknowledged for help with initial cell experiments.

The Research Council of Norway is acknowledged for the support to the Norwegian Micro- and Nano-Fabrication Facility, NorFab, project number 295864.

References

[1] Christian Frantz, Kathleen M. Stewart, and Valerie M. Weaver. "The extracellular matrix at a glance". In: *Journal of Cell Science* 123.24 (2010), pp. 4195–4200. DOI: 10.1242/jcs.023820.

[2] Molly M. Stevens and Julian H. George. "Exploring and engineering the cell surface interface." In: *Science* 310.November (2005), pp. 1135–1138. DOI: 10.1126/science.1106587.

[3] Marziye Mirbagheri et al. "Advanced cell culture platforms: a growing quest for emulating natural tissues". In: *Materials Horizons* 6.1 (2019), pp. 45–71. DOI: 10.1039/c8mh00803e.

[4] E. Cukierman et al. "Taking cell-matrix adhesions to the third dimension". In: *Science* 294.5547 (2001), pp. 1708–1712. DOI: 10.1126/science.1064829.

[5] Frederick Grinnell and W. Matthew Petroll. "Cell Motility and Mechanics in Three-Dimensional Collagen Matrices". In: *Annual Review of Cell and Developmental Biology* 26.1 (2010), pp. 335–361. DOI: 10.1146/annurev.cellbio.042308.113318.

[6] Brendon M. Baker and Christopher S. Chen. "Deconstructing the third dimension-how 3D culture microenvironments alter cellular cues". In: *Journal of Cell Science* 125.13 (2012), pp. 3015–3024. DOI: 10.1242/jcs.079509.

[7] Hongzhou Huang et al. "Peptide Hydrogelation and Cell Encapsulation for 3D Culture of MCF-7 Breast Cancer Cells". In: *PLoS ONE* 8.3 (Mar. 2013). Ed. by Adam J. Engler, e59482. DOI: 10.1371/journal.pone.0059482.

[8] Caleb Jensen and Yong Teng. "Is It Time to Start Transitioning From 2D to 3D Cell Culture?" In: *Frontiers in Molecular Biosciences* 7.March (2020), pp. 1–15. DOI: 10.3389/fmolb.2020.00033.

[9] Yanfen Li and Kristopher A. Kilian. "Bridging the Gap: From 2D Cell Culture to 3D Microengineered Extracellular Matrices". In: *Advanced Healthcare Materials* 4.18 (2015), pp. 2780–2796. DOI: 10.1002/adhm.201500427.

[10] Junzhe Lou et al. "Stress relaxing hyaluronic acid-collagen hydrogels promote cell spreading, fiber remodeling, and focal adhesion formation in 3D cell culture". In: *Biomaterials* 154 (2018), pp. 213–222. DOI: 10.1016/j.biomaterials.2017.11.004.

[11] Santiago Campuzano and Andrew E Pelling. "Scaffolds for 3D Cell Culture and Cellular Agriculture Applications Derived From Non-animal Sources". In: *Frontiers in Sustainable Food Systems* 3.38 (May 2019), pp. 1–9. DOI: 10.3389/fsufs.2019.00038.

[12] Ryosuke Ogaki, Morgan Alexander, and Peter Kingshott. "Chemical patterning in biointerface science". In: *Materials Today* 13.4 (Apr. 2010), pp. 22–35. DOI: 10.1016/S1369-7021(10)70057-2.

[13] Verónica Hortigüela et al. "Large-Area Biomolecule Nanopatterns on Diblock Copolymer Surfaces for Cell Adhesion Studies". In: *Nanomaterials* 9.4 (2019), p. 579. DOI: 10.3390/nano9040579.

[14] Shengwang Zhou et al. "Photoactivatable Reaction for Covalent Nanoscale Patterning of Multiple Proteins". In: *ACS Applied Materials and Interfaces* 10.47 (2018), pp. 40452–40459. DOI: 10.1021/acsami.8b16736.

[15] Yi Chun Yeh et al. "Mechanotransduction of matrix stiffness in regulation of focal adhesion size and number: Reciprocal regulation of caveolin-1 and β1 integrin". In: *Scientific Reports* 7.1 (2017), pp. 1–14. DOI: 10.1038/s41598-017-14932-6.

[16] Yvonne K Girard et al. "A 3D Fibrous Scaffold Inducing Tumoroids: A Platform for Anticancer Drug Development". In: *PLoS ONE* 8.10 (2013), e75345. DOI: 10.1371/journal.pone.0075345.

[17] Stuart G. Higgins et al. "High-Aspect-Ratio Nanostructured Surfaces as Biological Metamaterials". In: *Advanced Materials* 32.9 (2020), pp. 1–44. DOI: 10.1002/adma.201903862.

[18] Elsie S. Place, Nicholas D. Evans, and Molly M. Stevens. "Complexity in biomaterials for tissue engineering". In: *Nature Materials* 8.6 (2009), pp. 457–470. DOI: 10.1038/nmat2441.

[19] Douglas B Weibel, Willow R Diluzio, and George M Whitesides. "Microfabrication meets microbiology." In: *Nature reviews. Microbiology* 5.3 (2007), pp. 209–218. DOI: 10.1038/nrmicro1616.

[20] Paula M. Mendes. "Cellular nanotechnology: Making biological interfaces smarter". In: *Chemical Society Reviews* 42.24 (2013), pp. 9207–9218. DOI: 10.1039/c3cs60198f.

[21] Francesco Pampaloni, Emmanuel G Reynaud, and Ernst H K Stelzer. "Air-liquid interface Growth medium Apoptosis/anoikis Aggregation Polarization Differentiation". In: *Nature Reviews Molecular Cell Biology* 8.october (2007), pp. 839–845.

[22] Lisa A. Gurski et al. "3D Matrices for Anti-Cancer Drug Testing and Development". In: *Oncology Issues* 25.1 (Jan. 2010), pp. 20–25. DOI: 10.1080/10463356.2010.11883480.

[23] Sigrid A. Langhans. "Three-dimensional in vitro cell culture models in drug discovery and drug repositioning". In: *Frontiers in Pharmacology* 9.JAN (Jan. 2018), p. 6. DOI: 10.3389/fphar.2018.00006.

[24] Jiaxian Wang et al. "Effect of engineered anisotropy on the susceptibility of human pluripotent stem cell-derived ventricular cardiomyocytes to arrhythmias". In: *Biomaterials* 34.35 (2013), pp. 8878–8886. DOI: 10.1016/j.biomaterials.2013.07.039.

[25] Jesus Isaac Luna et al. "Multiscale biomimetic topography for the alignment of neonatal and embryonic stem cell-derived heart cells". In: *Tissue Engineering - Part C: Methods* 17.5 (2011), pp. 579–588. DOI: 10.1089/ten.tec.2010.0410.

[26] Benjamin Geiger et al. "Transmembrane extracellular matrix-cytoskeleton crosstalk". In: *Nature Reviews Molecular Cell Biology* 2.11 (Nov. 2001), pp. 793–805. DOI: 10.1038/35099066.

[27] Kenneth M. Yamada and Benjamin Geiger. "Molecular interactions in cell adhesion complexes". In: *Current Opinion in Cell Biology* 9.1 (1997), pp. 76–85. DOI: 10.1016/S0955-0674(97)80155-X.

[28] Wolfgang H. Goldmann. "Role of vinculin in cellular mechanotransduction". In: *Cell Biology International* 40.3 (Mar. 2016), pp. 241–256. DOI: 10.1002/cbin.10563.

[29] Zhiqi Sun, Mercedes Costell, and Reinhard Fässler. "Integrin activation by talin, kindlin and mechanical forces". In: *Nature Cell Biology* 21.1 (Jan. 2019), pp. 25–31. DOI: 10.1038/s41556-018-0234-9.

[30] Robert M. Ezzell et al. "Vinculin promotes cell spreading by mechanically coupling integrins to the cytoskeleton". In: *Experimental Cell Research* 231.1 (1997), pp. 14–26. DOI: 10.1006/excr.1996.3451.

[31] Peter M. Thompson et al. "Identification of an actin binding surface on vinculin that mediates mechanical cell and focal adhesion properties". In: *Structure* 22.5 (2014), pp. 697–706. DOI: 10.1016/j.str.2014.03.002.

[32] Ingo Thievessen et al. "Vinculin-actin interaction couples actin retrograde flow to focal adhesions, but is dispensable for focal adhesion growth". In: *Journal of Cell Biology* 202.1 (2013), pp. 163–177. DOI: 10.1083/jcb.201303129.

[33] Claudia Tanja Mierke et al. "Mechano-coupling and regulation of contractility by the vinculin tail domain". In: *Biophysical Journal* 94.2 (2008), pp. 661–670. DOI: 10.1529/biophysj.107.108472.

[34] Caitlin E. Tolbert, Keith Burridge, and Sharon L. Campbell. "Vinculin regulation of F-actin bundle formation". In: *Cell Adhesion & Migration* 7.2 (2013), pp. 219–225. DOI: 10.4161/cam.23184.

[35] Caitlin E. Tolbert et al. "Correction to Phosphorylation at Y1065 in Vinculin Mediates Actin Bundling, Cell Spreading, and Mechanical Responses to Force". In: *Biochemistry* 53.39 (2014), pp. 6286–6286. DOI: 10.1021/bi501135k.

[36] Kai Shen et al. "The vinculin C-terminal hairpin mediates F-actin bundle formation, focal adhesion, and cell mechanical properties". In: *Journal of Biological Chemistry* 286.52 (2011), pp. 45103–45115. DOI: 10.1074/jbc.M111.244293.

[37] Kuo Kuang Wen, Peter A. Rubenstein, and Kris A. DeMali. "Vinculin nucleates actin polymerization and modifies actin filament structure". In: *Journal of Biological Chemistry* 284.44 (2009), pp. 30463–30473. DOI: 10.1074/jbc.M109.021295.

[38] Christophe Le Clainche et al. "Vinculin is a dually regulated actin filament barbed end-capping and side-binding protein". In: *Journal of Biological Chemistry* 285.30 (2010), pp. 23420–23432. DOI: 10.1074/jbc.M110.102830.

[39] Kris A. DeMali, Christy A. Barlow, and Keith Burridge. "Recruitment of the Arp2/3 complex to vinculin: Coupling membrane protrusion to matrix adhesion". In: *Journal of Cell Biology* 159.5 (2002), pp. 881–891. DOI: 10.1083/jcb.200206043.

[40] Sangmyung Rhee et al. "Microtubule function in fibroblast spreading is modulated according to the tension state of cell-matrix interactions". In: *Proceedings of the National Academy of Sciences* 104.13 (Mar. 2007), pp. 5425–5430. DOI: 10.1073/pnas.0608030104.

[41] Kenneth M. Yamada and Michael Sixt. "Mechanisms of 3D cell migration". In: *Nature Reviews Molecular Cell Biology* 20.12 (2019), pp. 738–752. DOI: 10.1038/s41580-019-0172-9.

[42] Stephanie I. Fraley et al. "A distinctive role for focal adhesion proteins in three-dimensional cell motility". In: *Nature Cell Biology* 12.6 (2010), pp. 598–604. DOI: 10.1038/ncb2062.

[43] Magdalena A. Stolarska and Aravind R. Rammohan. "Center or periphery? Modeling the effects of focal adhesion placement during cell spreading". In: *PLoS ONE* 12.2 (2017), pp. 1–22. DOI: 10.1371/journal.pone.0171430.

[44] Muhammad H Zaman et al. "Migration of tumor cells in 3D matrices is governed by matrix stiffness along with cell-matrix adhesion and proteolysis". In: *Proceedings of the National Academy of Sciences* 103.29 (July 2006), pp. 10889–10894. DOI: 10.1073/pnas.0604460103.

[45] Jiranuwat Sapudom et al. "The phenotype of cancer cell invasion controlled by fibril diameter and pore size of 3D collagen networks". In: *Biomaterials* 52.1 (2015), pp. 367–375. DOI: 10.1016/j.biomaterials.2015.02.022.

[46] Jing Xie et al. "Collagen Gels with Different Fibrillar Microarchitectures Elicit Different Cellular Responses". In: *ACS Applied Materials and Interfaces* 9.23 (2017), pp. 19630–19637. DOI: 10.1021/acsami.7b03883.

[47] Kai S. Beckwith et al. "Influence of Nanopillar Arrays on Fibroblast Motility, Adhesion, and Migration Mechanisms". In: *Small* 15.43 (Aug. 2019), p. 1902514. DOI: 10.1002/smll.201902514.

[48] Allister F. McGuire, Francesca Santoro, and Bianxiao Cui. "Interfacing Cells with Vertical Nanoscale Devices: Applications and Characterization". In: *Annual Review of Analytical Chemistry* 11.1 (June 2018), pp. 101–126. DOI: 10.1146/annurev-anchem-061417-125705.

[49] S Bonde et al. "Exploring arrays of vertical one-dimensional nanostructures for cellular investigations". In: *Nanotechnology* 25.36 (2014), p. 362001. DOI: 10.1088/0957-4484/25/36/362001.

[50] Kai Sandvold Beckwith et al. "Tunable high aspect ratio polymer nanostructures for cell interfaces". In: *Nanoscale* 7.18 (2015), pp. 8438–8450. DOI: 10.1039/C5NR00674K.

[51] Xiao Li et al. "A nanostructure platform for live cell manipulation of membrane curvature". In: *Nature Protocols* 14.6 (2019), p. 1772. DOI: 10.1038/s41596-019-0161-7.

[52] Christelle N Prinz. "Interactions between semiconductor nanowires and living cells." In: *Journal of physics. Condensed matter : an Institute of Physics journal* 27.23 (2015), p. 233103. DOI: 10.1088/0953-8984/27/23/233103.

[53] Katrine R Rostgaard et al. "Vertical nanowire arrays as a versatile platform for protein detection and analysis". In: *Nanoscale* 5.21 (2013), p. 10226. DOI: 10.1039/c3nr03113f.

[54] Michele Dipalo et al. "Cells Adhering to 3D Vertical Nanostructures: Cell Membrane Reshaping without Stable Internalization". In: *Nano Letters* 18.9 (Sept. 2018), pp. 6100–6105. DOI: 10.1021/acs.nanolett.8b03163.

[55] Jing Dai et al. "Cellular architecture response to aspect ratio tunable nanoarrays". In: *Nanoscale* 12.23 (2020), pp. 12395–12404. DOI: 10.1039/d0nr01003k.

[56] Xi Xie et al. "Nanostraw-electroporation system for highly efficient intracellular delivery and transfection". In: *ACS Nano* 7.5 (2013), pp. 4351–4358. DOI: 10.1021/nn400874a.

[57] Elad Peer et al. "Hollow nanoneedle array and its utilization for repeated administration of biomolecules to the same cells". In: *ACS Nano* 6.6 (2012), pp. 4940–4946. DOI: 10.1021/nn300443h.

[58] Yu-Ran Na et al. "Probing Enzymatic Activity inside Living Cells Using a Nanowire–Cell "Sandwich" Assay". In: *Nano Letters* 13.1 (Jan. 2013), pp. 153–158. DOI: 10.1021/nl3037068.

[59] Lindsey Hanson et al. "Vertical nanopillars for in situ probing of nuclear mechanics in adherent cells". In: *Nature Nanotechnology* 10.6 (2015), pp. 554–562. DOI: 10.1038/nnano.2015.88. arXiv: 15334406.

[60] Hsin Ya Lou et al. "Membrane curvature underlies actin reorganization in response to nanoscale surface topography". In: *Proceedings of the National Academy of Sciences of the United States of America* 116.46 (Nov. 2019), pp. 23143–23151. DOI: 10.1073/pnas.1910166116.

[61] Hsin Ya Lou et al. "The Role of Membrane Curvature in Nanoscale Topography-Induced Intracellular Signaling". In: *Accounts of Chemical Research* 51.5 (2018), pp. 1046–1053. DOI: 10.1021/acs.accounts.7b00594.

[62] Wenting Zhao et al. "Nanoscale manipulation of membrane curvature for probing endocytosis in live cells". In: *Nature Nanotechnology* 12.8 (June 2017), pp. 750–756. DOI: 10.1038/nnano.2017.98.

[63] Jakob Vinje, Kai S. Beckwith, and Pawel Sikorski. "Electron Beam Lithography Fabrication of SU-8 Polymer Structures for Cell Studies". In: *Journal of Microelectromechanical Systems* 29.2 (Apr. 2020), pp. 160–169. DOI: 10.1109/JMEMS.2020.2967174.

[64] F. L. Van Rossum, G.; Drake. *Python 3 Reference Manual.* Vol. CreateSpac. Scotts Valley, CA: CreateSpace, 2009.

[65] Christoph Gohlke. *czifile*. Irvine, California, 2017.

[66] Pauli Virtanen et al. "SciPy 1.0: fundamental algorithms for scientific computing in Python". In: *Nature Methods* 17.3 (Mar. 2020), pp. 261–272. DOI: 10.1038/s41592-019-0686-2. arXiv: 1907.10121.

[67] Stefan Van Der Walt et al. "Scikit-image: Image processing in python". In: *PeerJ* 2014.1 (June 2014), e453. DOI: 10.7717/peerj.453.

[68] Sara Bonde et al. "Towards a better prediction of cell settling on nanostructure arrays - Simple means to complicated ends". In: *Advanced Functional Materials* 25.21 (2015), pp. 3246–3255. DOI: 10.1002/adfm.201500399.

[69] Nina Buch-Månson et al. "Mapping cell behavior across a wide range of vertical silicon nanocolumn densities". In: *Nanoscale* 9.17 (2017), pp. 5517–5527. DOI: 10.1039/c6nr09700f.

[70] Joseph Huff et al. "The new 2D Superresolution mode for ZEISS Airyscan". In: *Nature Methods* 14.12 (Dec. 2017), pp. 1223–1223. DOI: 10.1038/nmeth.f.404.

[71] Ariel Livne and Benjamin Geiger. "The inner workings of stress fibers - From contractile machinery to focal adhesions and back". In: *Journal of Cell Science* 129.7 (2016), pp. 1293–1304. DOI: 10.1242/jcs.180927.

[72] Masha Prager-Khoutorsky et al. "Fibroblast polarization is a matrix-rigidity-dependent process controlled by focal adhesion mechanosensing". In: *Nature Cell Biology* 13.12 (2011), pp. 1457–1465. DOI: 10.1038/ncb2370.

[73] Xi Xie et al. "Determining the Time Window for Dynamic Nanowire Cell Penetration Processes". In: *ACS Nano* 9.12 (2015), pp. 11667–11677. DOI: 10.1021/acsnano.5b05498.

[74] Ayush Verma and Francesco Stellacci. "Effect of Surface Properties on Nanoparticleâ€“Cell Interactions". In: *Small* 6.1 (Jan. 2010), pp. 12–21. DOI: 10.1002/smll.200901158.

[75] Piyush Verma, Ian Y. Wong, and Nicholas A. Melosh. "Continuum model of mechanical interactions between biological cells and artificial nanostructures". In: *Biointerphases* 5.2 (2010), pp. 37–44. DOI: 10.1116/1.3431960.

[76] Xi Xie et al. "Mechanical Model of Vertical Nanowire Cell Penetration". In: *Nano Letters* 13.12 (Dec. 2013), pp. 6002–6008. DOI: 10.1021/nl403201a.

[77] Drazen Raucher and Michael P. Sheetz. "Characteristics of a membrane reservoir buffering membrane tension". In: *Biophysical Journal* 77.4 (1999), pp. 1992–2002. DOI: 10.1016/S0006-3495(99)77040-2.

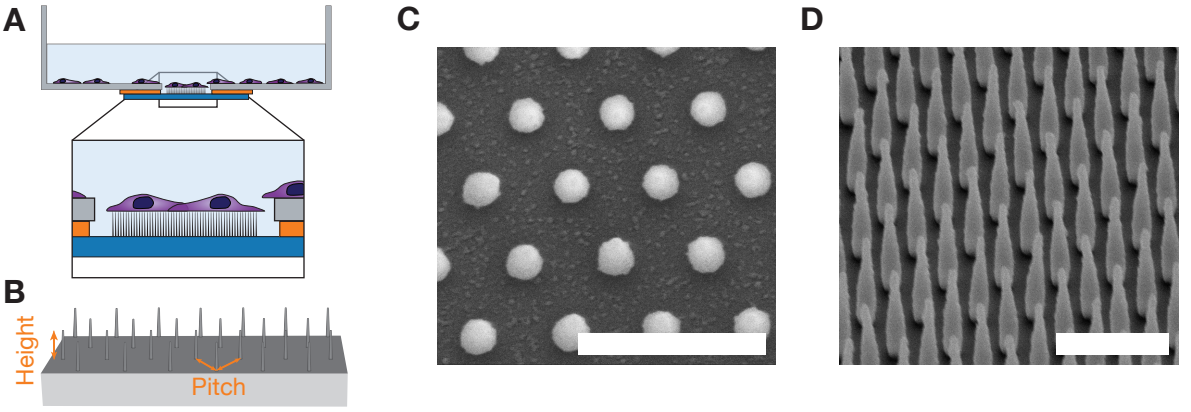
A
B
Height
Pitch
C
D

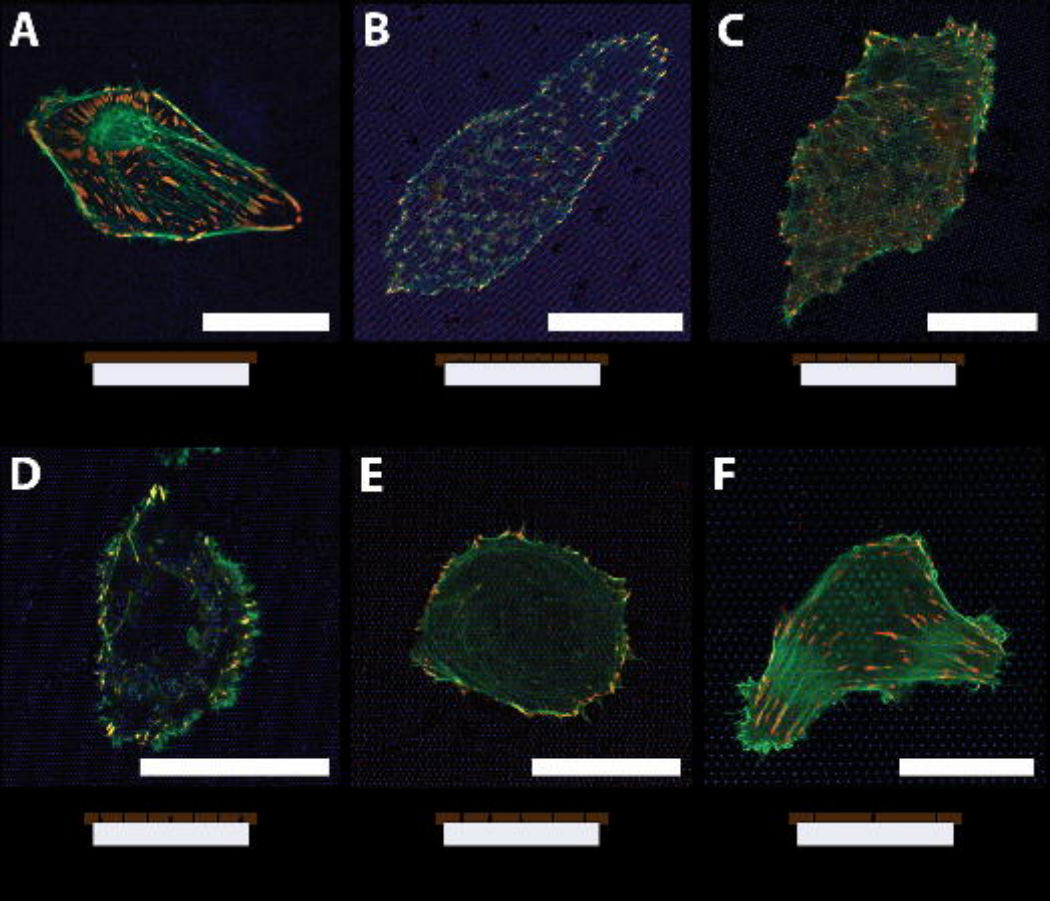
A
B
C
D
E
F

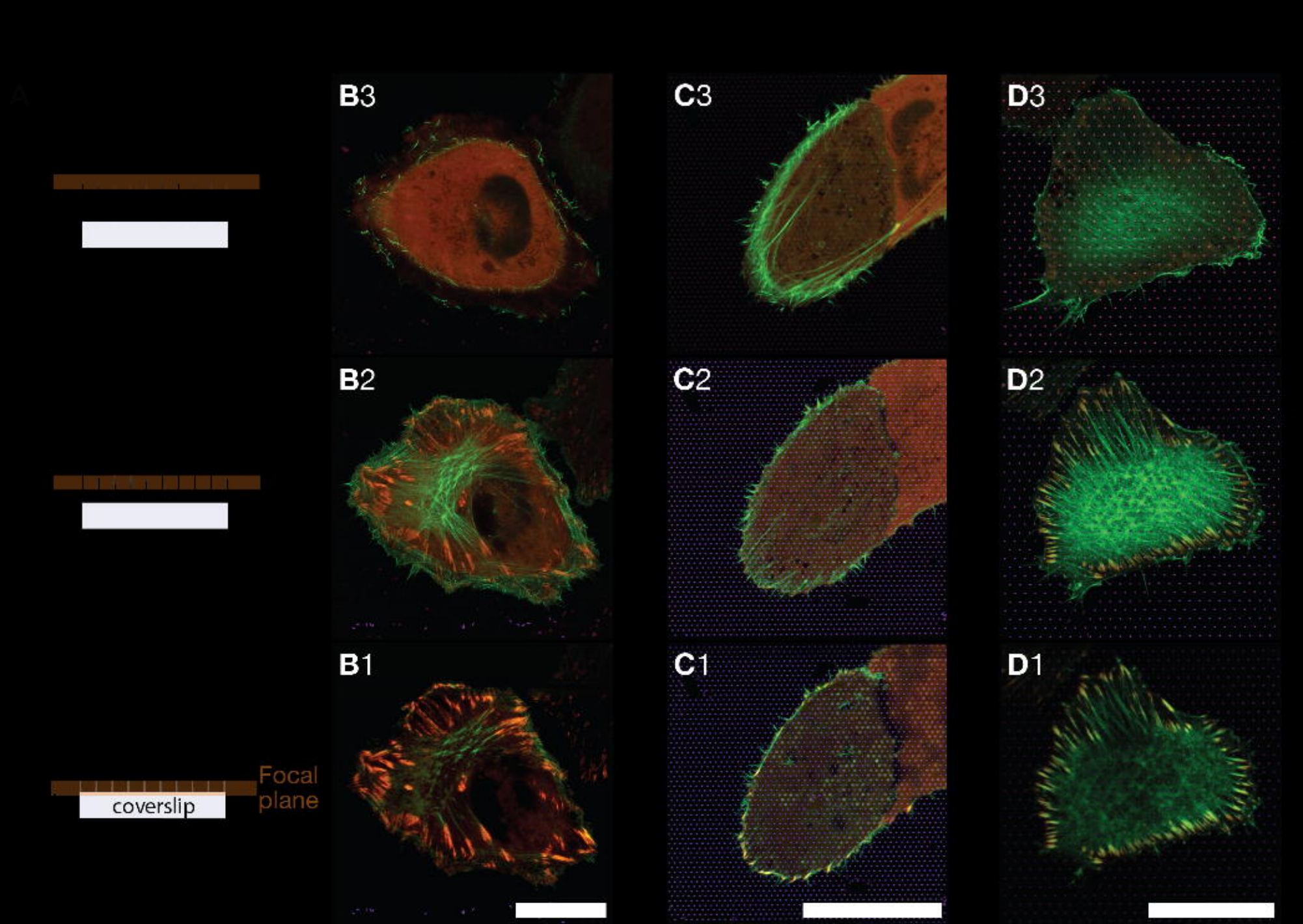
B3
C3
D3
B2
C2
D2
B1
C1
D1
Focal plane
coverslip

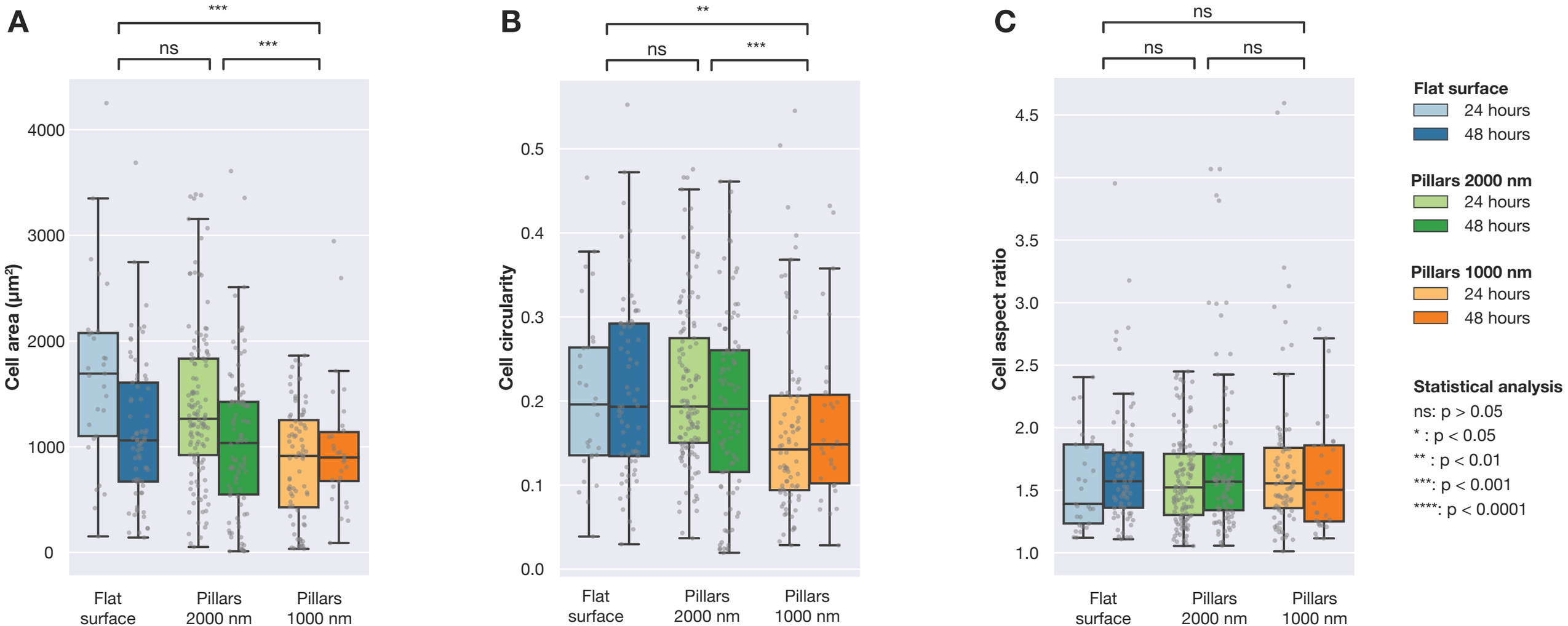
A
***
ns
***
Cell area (µm²)
4000
3000
2000
1000
0
Flat surface
Pillars 2000 nm
Pillars 1000 nm
B
**
ns
***
Cell circularity
0.5
0.4
0.3
0.2
0.1
0.0
Flat surface
Pillars 2000 nm
Pillars 1000 nm
C
ns
ns
ns
Cell aspect ratio
4.5
4.0
3.5
3.0
2.5
2.0
1.5
1.0
Flat surface
Pillars 2000 nm
Pillars 1000 nm
Flat surface
24 hours
48 hours
Pillars 2000 nm
24 hours
48 hours
Pillars 1000 nm
24 hours
48 hours
Statistical analysis
ns: p > 0.05
* : p < 0.05
** : p < 0.01
***: p < 0.001
****: p < 0.0001

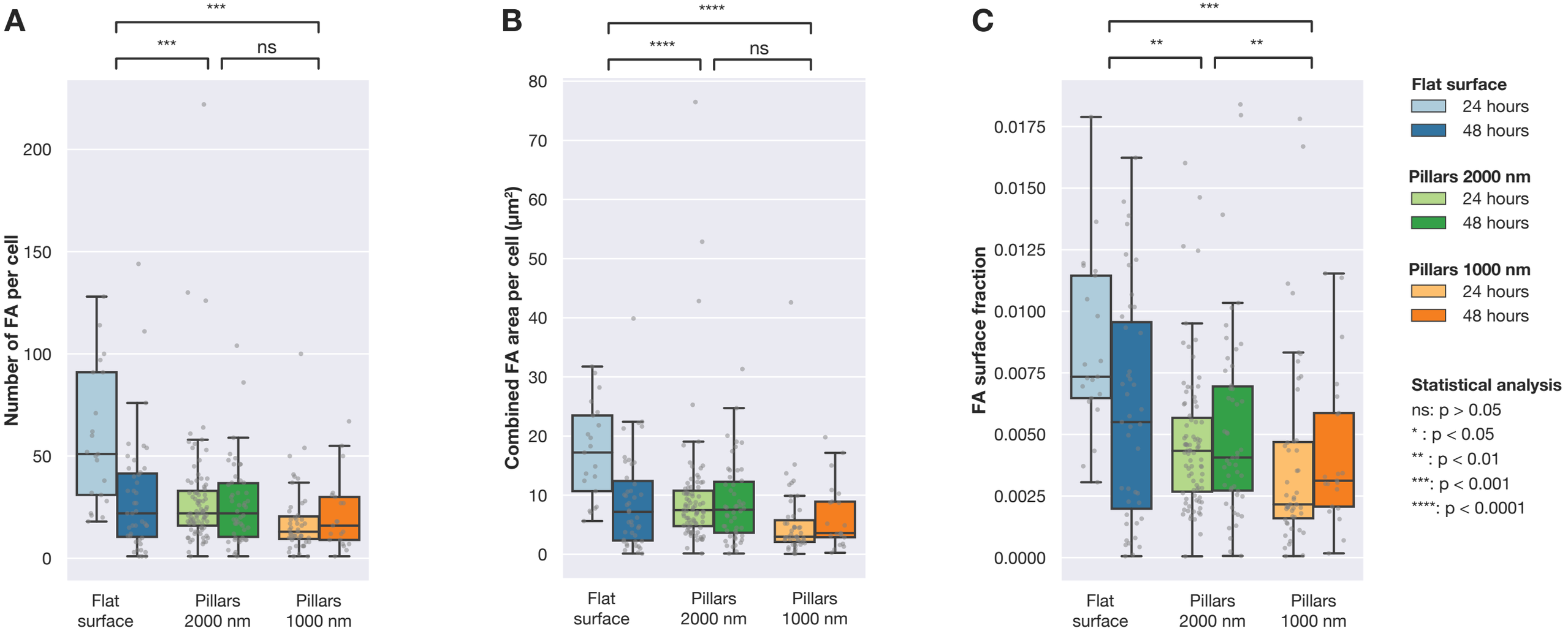
A
***
***
ns
Number of FA per cell
0
50
100
150
200
Flat surface
Pillars 2000 nm
Pillars 1000 nm
B
****
****
ns
Combined FA area per cell (µm²)
0
10
20
30
40
50
60
70
80
Flat surface
Pillars 2000 nm
Pillars 1000 nm
C
***
**
**
FA surface fraction
0.0000
0.0025
0.0050
0.0075
0.0100
0.0125
0.0150
0.0175
Flat surface
Pillars 2000 nm
Pillars 1000 nm
Flat surface
24 hours
48 hours
Pillars 2000 nm
24 hours
48 hours
Pillars 1000 nm
24 hours
48 hours
Statistical analysis
ns: p > 0.05
* : p < 0.05
** : p < 0.01
***: p < 0.001
****: p < 0.0001

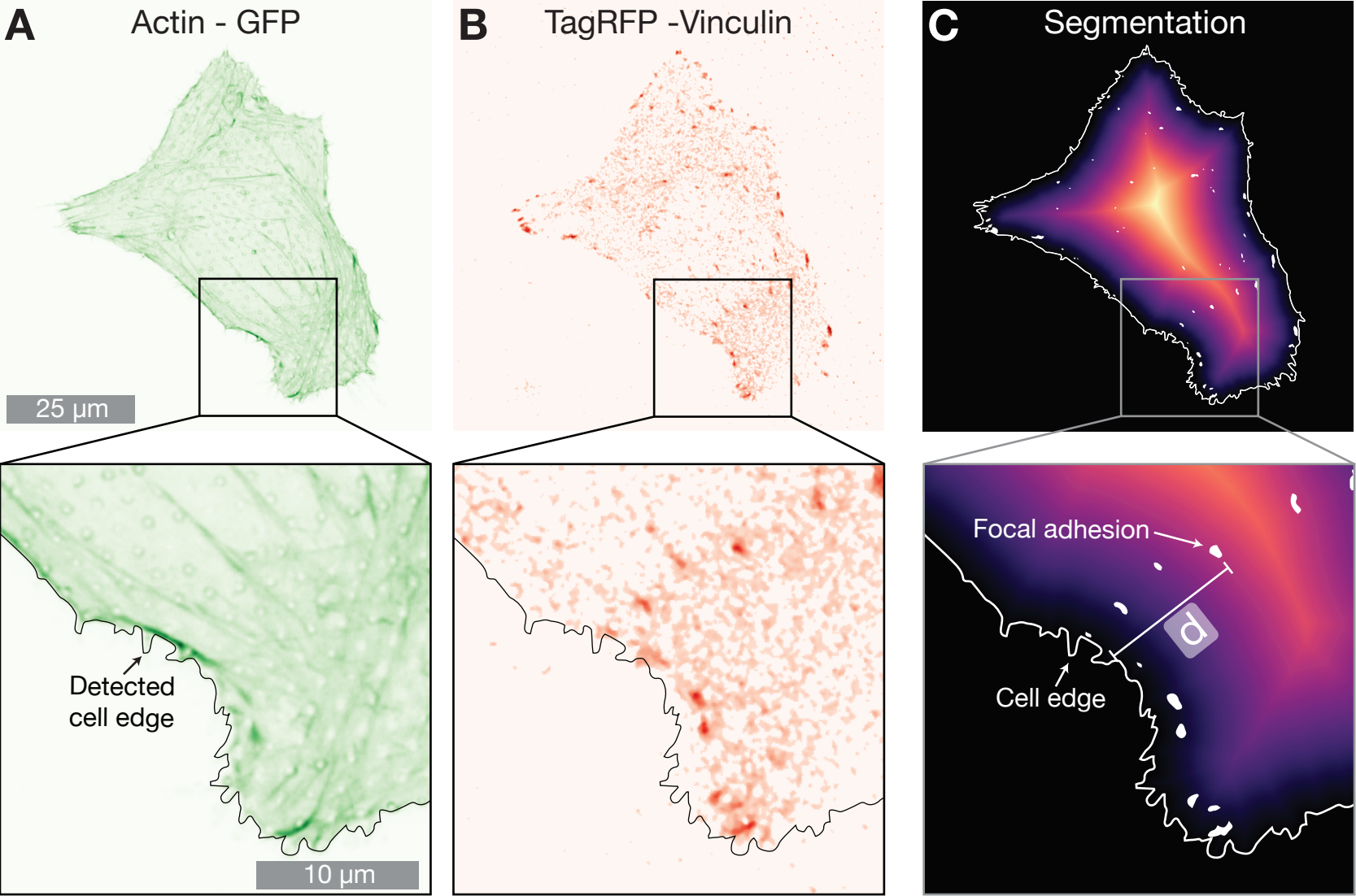
A
Actin - GFP
25 µm
Detected
cell edge
10 µm
B
TagRFP -Vinculin
C
Segmentation
Focal adhesion
d
Cell edge

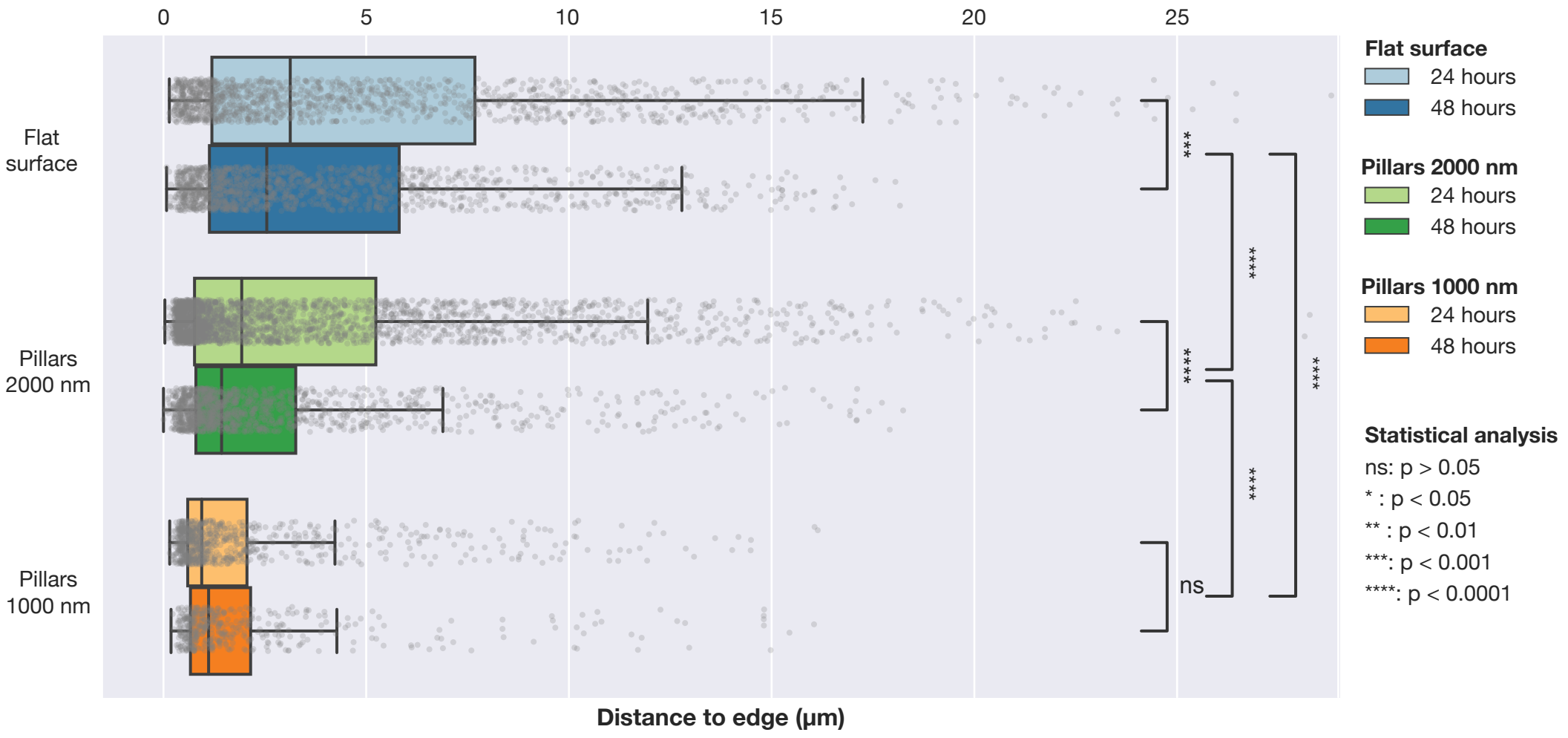
0
5
10
15
20
25
Flat surface
Pillars 2000 nm
Pillars 1000 nm
***
****
****
****
ns
Distance to edge (µm)
Flat surface
24 hours
48 hours
Pillars 2000 nm
24 hours
48 hours
Pillars 1000 nm
24 hours
48 hours
Statistical analysis
ns: p > 0.05
* : p < 0.05
** : p < 0.01
***: p < 0.001
****: p < 0.0001